Qu, Zengcai; Hinkkanen, Marko; Harnefors, Lennart

Gain scheduling of a full-order observer for sensorless induction motor drives

Published in:
IEEE Transactions on Industry Applications

DOI:
10.1109/TIA.2014.2323482

Published: 20/11/2014

Document Version
Peer-reviewed accepted author manuscript, also known as Final accepted manuscript or Post-print

Please cite the original version:
Qu, Z., Hinkkanen, M., & Harnefors, L. (2014). Gain scheduling of a full-order observer for sensorless induction motor drives. *IEEE Transactions on Industry Applications*, *50*(6), 3834-3845.
https://doi.org/10.1109/TIA.2014.2323482

Gain Scheduling of a Full-Order Observer for Sensorless Induction Motor Drives

Zengcai Qu, Marko Hinkkanen, *Senior Member, IEEE,* and Lennart Harnefors, *Senior Member, IEEE*

***Abstract*—This paper deals with the design of a speed-adaptive full-order observer for sensorless induction motor (IM) drives. A general stabilizing observer gain matrix, having three free design parameters, is used as a design framework. A gain-scheduled selection of the free design parameters is proposed. Furthermore, the full-order observer is augmented with the stator-resistance adaptation, and the local stability of the augmented observer is analyzed. The performance of the proposed full-order observer design is experimentally compared with a reduced-order observer using a 2.2-kW IM drive.**

***Index Terms*—Flux estimation, full-order observer, induction motor, resistance adaptation, sensorless, stability.**

I. Introduction

It is well known that instability phenomena can arise in sensorless control of induction motor (IM) drives, especially in the regenerative low-speed region [1] and also in high-speed operation [2]. The observer, which is used for estimating the flux and rotor speed, requires appropriate gains to avoid these problems. Tuning the gains is challenging, and local stability for all operating points (complete stability) is difficult to achieve, even if accurate parameter estimates are assumed. Furthermore, the observers are sensitive to errors in model parameters, particularly to the model stator resistance at low speeds.

Most sensorless estimators can be classified either as speed-adaptive observers [2]–[16] or inherently sensorless observers [17]–[21]. In both these classes, various observer structures and design approaches exist. For example, an artificial-neural-network based estimator [12], square-root-unscented Kalman filtering [15], robust Kalman filtering [16], and H_∞ theory [13] have recently been applied to the observer gain design. Comparatively simple, but still very flexible, observer structures are the speed-adaptive full-order observer [3] and the inherently sensorless variant [20], [21] of the classical reduced-order observer [22].

Properties of these different observers highly depend on their gains. Rigorous proof of the complete stability is available only for a few observer types [8], [9], [11], [20], [21]. A general stabilizing gain for the inherently sensorless reduced-order observer was presented in [20], [21]. The reduced-order observer is simpler to implement and tune than the full-order observer, but it can be more sensitive to noise at high speeds (for similar dynamic performance). The full-order observer has four degrees of freedom in the selection of the two observer gains, which complicates the design procedure. A general stabilizing observer gain matrix for the speed-adaptive full-order observer was derived in [9], where also a gain-scheduling design of three free design parameters was proposed. This original gain design guarantees sufficient damping at every operating point, but it leads to very high sensitivity to model parameter errors at lowest speeds.

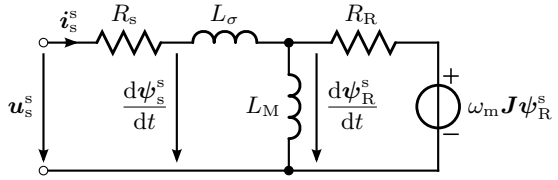

Fig. 1. Inverse-Γ model in stator coordinates.

Because the induced electromotive force (EMF) at low speeds is very small, the mismatch of the voltage drop across the stator resistance has a serious influence on the flux and speed estimation. To improve low-speed operation, the reduced-order observer can be augmented with a completely stable resistance-adaptation scheme [21]. On the other hand, the speed-adaptive full-order observers augmented with stator-resistance adaptation schemes have unstable regions (except in the case of some special observer structures [8], [11]).

In this paper, the observer gain design and the analysis of the stator-resistance adaptation for the speed-adaptive full-order observer are considered. The main contributions of the paper are:

1) A gain-scheduling design for the full-order observer is proposed, using the general stabilizing gain matrix given in [9] as a design framework. The proposed design improves the robustness against model parameter errors at lowest speeds. At higher speeds, the proposed design results in constant-valued gains, which provide sufficient damping.
2) The local stability of the full-order observer, augmented with the stator-resistance adaptation mechanism, is analyzed.
3) The proposed full-order observer design is experimentally compared with the original design [9] and the reduced-order observer design presented in [21] using a sensorless 2.2-kW IM drive.

The preliminary version of this paper was presented at the IEEE International Symposium on Sensorless Control for Electrical Drives and Predictive Control of Electrical Drives and Power Electronics (SLED/PRECEDE 2013), Munich, Germany, Oct. 17–19, 2013.

Z. Qu and M. Hinkkanen are with Aalto University, Department of Electrical Engineering, P.O. Box 13000, FI-00076 Aalto, Espoo, Finland (e-mail: zengcai.qu@aalto.fi; marko.hinkkanen@aalto.fi).

L. Harnefors is with ABB Corporate Research, SE-72178 Västerås, Sweden (e-mail: lennart.harnefors@se.abb.com)

TABLE I
PARAMETERS OF THE 2.2-KW IM

Stator resistance R_s	0.064 p.u.
Rotor resistance R_R	0.040 p.u.
Leakage inductance L_σ	0.17 p.u.
Magnetizing inductance L_M	2.20 p.u.

II. IM MODEL

The inverse-Γ model of the IM shown in Fig. 1 is considered. The electrical dynamics in coordinates rotating at the angular speed $\hat{\omega}_\mathrm{s}$ of the rotor flux estimate are given by

$$\frac{\mathrm{d}}{\mathrm{d}t}\underbrace{\begin{bmatrix}\boldsymbol{i}_\mathrm{s}\\ \boldsymbol{\psi}_\mathrm{R}\end{bmatrix}}_{\boldsymbol{x}} = \underbrace{\begin{bmatrix}-\frac{R_\sigma}{L_\sigma}\boldsymbol{I}-\hat{\omega}_\mathrm{s}\boldsymbol{J} & \frac{1}{L_\sigma}(\alpha\boldsymbol{I}-\omega_\mathrm{m}\boldsymbol{J})\\ R_\mathrm{R}\boldsymbol{I} & -\alpha\boldsymbol{I}-(\hat{\omega}_\mathrm{s}-\omega_\mathrm{m})\boldsymbol{J}\end{bmatrix}}_{\boldsymbol{A}}\begin{bmatrix}\boldsymbol{i}_\mathrm{s}\\ \boldsymbol{\psi}_\mathrm{R}\end{bmatrix} + \underbrace{\begin{bmatrix}\frac{1}{L_\sigma}\boldsymbol{I}\\ \boldsymbol{O}\end{bmatrix}}_{\boldsymbol{B}}\boldsymbol{u}_\mathrm{s} \tag{1a}$$

$$\boldsymbol{i}_\mathrm{s} = \underbrace{\begin{bmatrix}\boldsymbol{I} & \boldsymbol{O}\end{bmatrix}}_{\boldsymbol{C}}\begin{bmatrix}\boldsymbol{i}_\mathrm{s}\\ \boldsymbol{\psi}_\mathrm{R}\end{bmatrix} \tag{1b}$$

where

$$\boldsymbol{I} = \begin{bmatrix}1 & 0\\ 0 & 1\end{bmatrix} \qquad \boldsymbol{J} = \begin{bmatrix}0 & -1\\ 1 & 0\end{bmatrix} \qquad \boldsymbol{O} = \begin{bmatrix}0 & 0\\ 0 & 0\end{bmatrix}$$

The space vector $\boldsymbol{i}_\mathrm{s} = [i_\mathrm{d}, i_\mathrm{q}]^\mathrm{T}$ is the stator current, $\boldsymbol{u}_\mathrm{s} = [u_\mathrm{d}, u_\mathrm{q}]^\mathrm{T}$ the stator voltage, and $\boldsymbol{\psi}_\mathrm{R} = [\psi_\mathrm{Rd}, \psi_\mathrm{Rq}]^\mathrm{T}$ the rotor flux. The total resistance is $R_\sigma = R_\mathrm{s} + R_\mathrm{R}$, where R_s is the stator resistance and R_R the rotor resistance. The leakage inductance is L_σ, the magnetizing inductance is L_M, the inverse rotor time constant is $\alpha = R_\mathrm{R}/L_\mathrm{M}$, and the electrical rotor speed is ω_m.

A 2.2-kW 400-V IM will be considered in the following analysis and experiments. The rating of the motor is as follows: speed 1436 r/min; frequency 50 Hz; line-to-line rms voltage 400 V; rms current 5 A; and torque 14.6 Nm. The per-unit (p.u.) quantities will be used; the base values for angular speed, voltage, and current are defined as $2\pi\cdot 50$ rad/s, $\sqrt{2/3}\cdot 400$ V, and $\sqrt{2}\cdot 5$ A, respectively. The p.u. model parameters of the IM are given in Table I. It is worth mentioning that the same (or very similar) p.u. values of the observer tuning parameters can be used for different machines. Naturally, the tuning parameters differ significantly, if they are not normalized.

III. SPEED-ADAPTIVE FULL-ORDER FLUX OBSERVER

A. Observer Structure

The speed-adaptive full-order observer is expressed as [3]

$$\frac{\mathrm{d}\hat{\boldsymbol{x}}}{\mathrm{d}t} = \hat{\boldsymbol{A}}\hat{\boldsymbol{x}} + \boldsymbol{B}\boldsymbol{u}_\mathrm{s} + \boldsymbol{K}(\boldsymbol{i}_\mathrm{s} - \hat{\boldsymbol{i}}_\mathrm{s}) \tag{2a}$$

$$\hat{\boldsymbol{i}}_\mathrm{s} = \boldsymbol{C}\hat{\boldsymbol{x}} \tag{2b}$$

where "$\hat{}$" denotes the estimated values. The state estimate and the observer system matrix are

$$\hat{\boldsymbol{x}} = \begin{bmatrix}\hat{\boldsymbol{i}}_\mathrm{s}\\ \hat{\boldsymbol{\psi}}_\mathrm{R}\end{bmatrix}, \quad \hat{\boldsymbol{A}} = \begin{bmatrix}-\frac{\hat{R}_\sigma}{L_\sigma}\boldsymbol{I}-\hat{\omega}_\mathrm{s}\boldsymbol{J} & \frac{1}{L_\sigma}(\alpha\boldsymbol{I}-\hat{\omega}_\mathrm{m}\boldsymbol{J})\\ R_\mathrm{R}\boldsymbol{I} & -\alpha\boldsymbol{I}-(\hat{\omega}_\mathrm{s}-\hat{\omega}_\mathrm{m})\boldsymbol{J}\end{bmatrix}$$

respectively, where the total resistance estimate is $\hat{R}_\sigma = \hat{R}_\mathrm{s} + R_\mathrm{R}$. The observer gain matrix is

$$\boldsymbol{K} = \begin{bmatrix}\boldsymbol{K}_\mathrm{s}\\ \boldsymbol{K}_\mathrm{r}\end{bmatrix} = \begin{bmatrix}k_\mathrm{sd}\boldsymbol{I} + k_\mathrm{sq}\boldsymbol{J}\\ k_\mathrm{rd}\boldsymbol{I} + k_\mathrm{rq}\boldsymbol{J}\end{bmatrix} \tag{3}$$

The rotor speed estimate is obtained using the conventional adaptation law

$$\hat{\omega}_\mathrm{m} = k_\mathrm{p}\hat{\boldsymbol{\psi}}_\mathrm{R}^\mathrm{T}\boldsymbol{J}\tilde{\boldsymbol{i}}_\mathrm{s} + \int k_\mathrm{i}\hat{\boldsymbol{\psi}}_\mathrm{R}^\mathrm{T}\boldsymbol{J}\tilde{\boldsymbol{i}}_\mathrm{s}\mathrm{d}t \tag{4}$$

where k_p and k_i are the speed adaptation gains. The current estimation error $\tilde{\boldsymbol{i}}_\mathrm{s} = \boldsymbol{i}_\mathrm{s} - \hat{\boldsymbol{i}}_\mathrm{s}$, and estimation errors of other variables are marked similarly. If the observer is implemented in estimated flux coordinates, the flux estimate is $\hat{\boldsymbol{\psi}}_\mathrm{R} = [\hat{\psi}_\mathrm{R}, 0]^\mathrm{T}$. In these coordinates, the speed adaptation law (4) reduces to

$$\hat{\omega}_\mathrm{m} = k_\mathrm{p}\hat{\psi}_\mathrm{R}\tilde{i}_\mathrm{q} + \int k_\mathrm{i}\hat{\psi}_\mathrm{R}\tilde{i}_\mathrm{q}\mathrm{d}t \tag{5}$$

B. Gain Design

The general stabilizing observer gains in (3) are [9]

$$\boldsymbol{K}_\mathrm{s} = \frac{r - \hat{R}_\sigma}{L_\sigma}\boldsymbol{I} + \frac{x}{L_\sigma}\boldsymbol{J} \tag{6a}$$

$$\boldsymbol{K}_\mathrm{r} = (R_\mathrm{R} - r + \alpha l)\boldsymbol{I} + (\hat{\omega}_\mathrm{m} l - x)\boldsymbol{J} \tag{6b}$$

where $l > 0$, $r > 0$, and x can be freely chosen.[1] With these gains, the closed-loop estimation error dynamics are locally stable at any operating point (for positive k_p and k_i).

The design framework (6) will be used in the following. Even if (6) guarantees complete stability for accurate parameter estimates, the selection of the free design parameters l, r, and x significantly affects the robustness, damping, convergence rate, and other properties of the system. In order to achieve good performance, it is necessary to vary these parameters as a function of the speed estimate (or the stator frequency).

1) Original Design: In [9], the goal in the selection of the free design parameters has been to guarantee sufficient damping for all operating points. The relationships between the design parameters l, r, and x and approximate open- and closed-loop pole locations have been derived. Based on these relationships, the following parameters were given:

$$l = L_\sigma\frac{\hat{\omega}_\mathrm{s}^2}{\alpha^2 + \hat{\omega}_\mathrm{m}^2} \tag{7a}$$

$$r = L_\sigma\cdot\max\{|\hat{\omega}_\mathrm{s}|, \omega_\mathrm{min}\} \tag{7b}$$

$$x = 0 \tag{7c}$$

where ω_min is a design constant. In the following, $\omega_\mathrm{min} = 0.1$ p.u. is used.

The speed adaptation gains were selected as

$$k_\mathrm{i} = \frac{2T_\mathrm{N}}{J\delta}\frac{|\hat{\omega}_\mathrm{s}|L_\sigma}{\hat{\psi}_\mathrm{R}^2} \qquad k_\mathrm{p} = \frac{k_\mathrm{i}L_\sigma}{r} \tag{8}$$

[1]The notation used in this paper differs from [9]: $l = k_2'$, $r = L_\sigma x'$, $x = L_\sigma(\hat{\omega}_\mathrm{m} + y')$, where the original parameters are marked with the prime. This different notation is selected in order to highlight the physical nature of these parameters: l can be considered as a virtual inductance, r as a virtual resistance, and x as a virtual reactance.

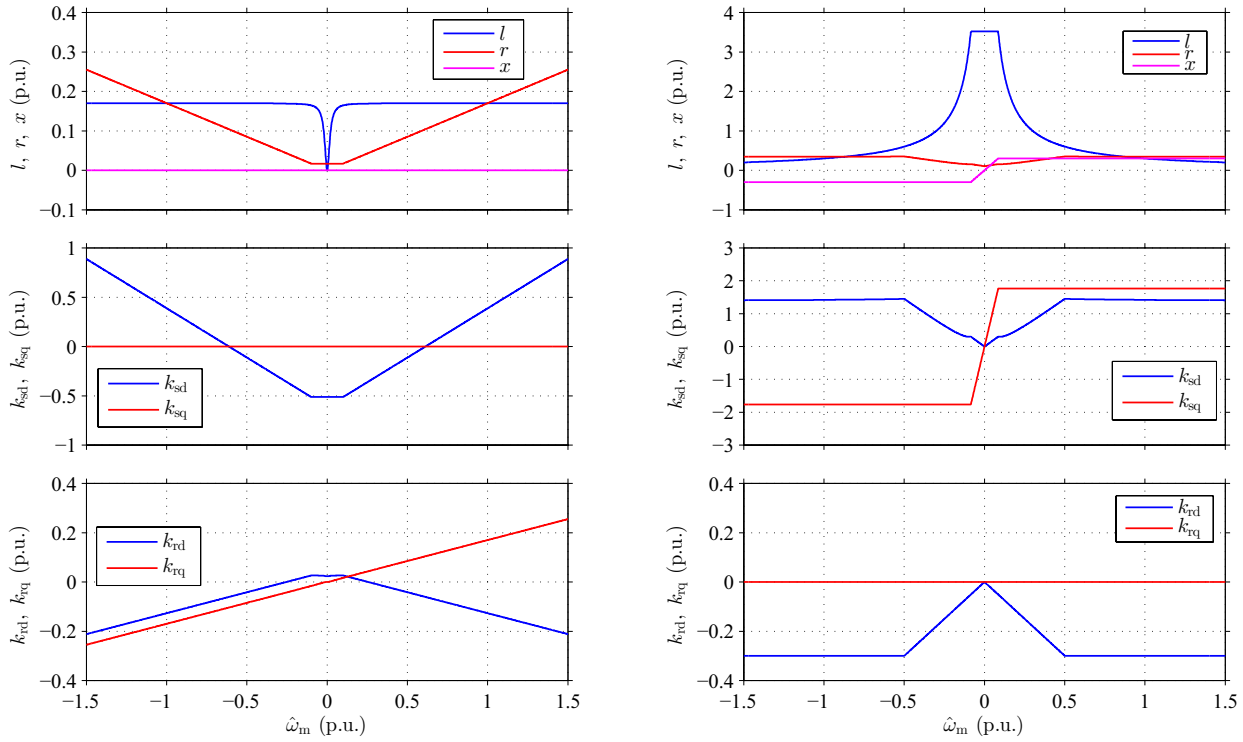

(a) (b)

Fig. 2. Gain designs: (a) original design; (b) proposed design. The first subplot shows the design parameters l, r, and x; the second and third subplots show the resulting observer gain components as function of $\hat{\omega}_\mathrm{m}$.

where J is the total moment of inertia and the design constant δ can be interpreted as the specified speed tracking error during the ramp acceleration under the rated torque T_N. It can be seen that k_i is proportional to the stator frequency $\hat{\omega}_\mathrm{s}$ and inversely proportional to the square $\hat{\psi}_\mathrm{R}^2$ of the estimated flux magnitude. The speed adaptation gain can be formulated as $k_\mathrm{i} = k_\mathrm{i}'|\hat{\omega}_\mathrm{s}|/\hat{\psi}_\mathrm{R}^2$, where $k_\mathrm{i}' = 2T_\mathrm{N}L_\sigma/J\delta$ is a design constant. In the following, $k_\mathrm{i}' = 0.5$ p.u. is used.

The design parameters l, r, and x as well as the resulting components of $\boldsymbol{K}_\mathrm{s}$ and $\boldsymbol{K}_\mathrm{r}$ as function of $\hat{\omega}_\mathrm{m}$ are shown in Fig. 2(a). As shown in Appendix A, the dynamics of the observer become equivalent to those of the pure voltage model at zero stator frequency (since $l = 0$ at $\hat{\omega}_\mathrm{s} = 0$). Due to this undesirable feature, the drive cannot be operated at zero frequency without load (i.e., dc magnetization), which complicates the starting of the drive. Furthermore, the observer design is very sensitive to the errors in $\hat{R}_\mathrm{s}$ at low frequencies due to the voltage-model-like behavior, which may cause serious problems, e.g., in speed reversals.

The nonlinear estimation-error dynamics are governed by (1) and (2) together with the speed-adaptation law (4). Local dynamic properties of this nonlinear system can be studied by means of the linearized model (Appendix B). The eigenvalues of the linearized estimation-error dynamics with the original gain design are shown in Fig. 12(a). It can be seen that the damping is sufficient at all speeds.

2) Proposed Design: The observer gain proposed in [4]

$$\boldsymbol{K}_\mathrm{s} = \frac{z + |\hat{\omega}_\mathrm{s}|L_\sigma - \hat{R}_\sigma}{L_\sigma}\boldsymbol{I} \tag{9a}$$

$$\boldsymbol{K}_\mathrm{r} = [R_\mathrm{R} - z \cdot f(\hat{\omega}_\mathrm{s})]\,\boldsymbol{I} + z \cdot f(\hat{\omega}_\mathrm{s}) \cdot \mathrm{sign}(\hat{\omega}_\mathrm{s})\boldsymbol{J} \tag{9b}$$

yields well-damped and comparatively robust estimation-error dynamics at higher speeds. The function f is shown in Fig. 4, and it can be expressed as

$$f(\omega) = \min\left\{\frac{|\omega|}{\omega_\Delta}, 1\right\} \tag{10}$$

The tuning parameters z and ω_Δ are positive constants.[2]

The drawback of (9) is that an unstable region at low speeds in the regenerating mode exists [20]. In the proposed design, the free parameters of (6) are selected so that the observer gains at higher speeds resemble those in (9). This goal can be achieved by choosing

$$l = \min\left\{\frac{R_\mathrm{s}}{\alpha}, \frac{z}{|\hat{\omega}_\mathrm{m}|}\right\} \tag{11a}$$

$$r = R_\mathrm{R} + \alpha l + z \cdot f(\hat{\omega}_\mathrm{m}) \tag{11b}$$

$$x = \hat{\omega}_\mathrm{m} l \tag{11c}$$

where the function f given in (10) depends on $\hat{\omega}_\mathrm{m}$. As an example, the design parameters l, r, and x as well as the resulting components of $\boldsymbol{K}_\mathrm{s}$ and $\boldsymbol{K}_\mathrm{r}$ as function of $\hat{\omega}_\mathrm{m}$ are shown in Fig. 2(b), where the two positive design constants are selected as: $\omega_\Delta = 0.5$ p.u. and $z = 0.3$ p.u. It can be seen

[2]The scaling of the tuning parameter z differs slightly from the original paper: $z = \alpha' L_\sigma$, where α' refers to the tuning parameter used in [4].

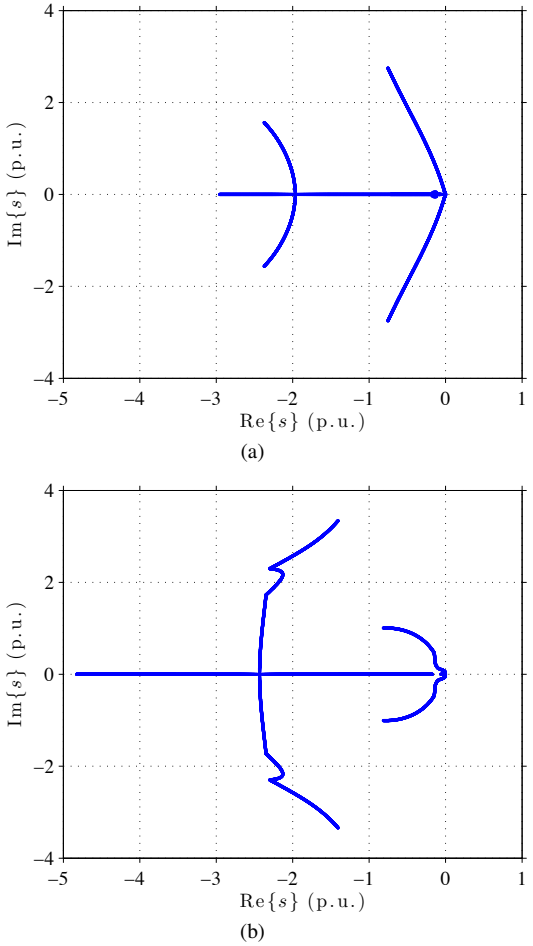

Fig. 3. Eigenvalues of the closed-loop system matrix: (a) original gain design; (b) proposed gain design. The operating-point stator frequency is varied as $\omega_{\mathrm{s}0} = 0 \ldots 2$ p.u. and the slip frequency corresponds to the rated load. In both cases, all the eigenvalues stay in the left-half plane also at the smallest speeds in every load conditions due to the design framework [9].

that l is always positive, and the voltage-model behavior is avoided. Furthermore, it can be seen that the gains are constant at speeds higher than ω_Δ. It is to be noted that both $x = 0$ and $x = \hat{\omega}_{\mathrm{m}} l$ lead to simple observer gain components, cf. (6). The selection given in (11c) was made based on the damping.

The speed adaptation gains are selected as

$$k_{\mathrm{i}} = k'_{\mathrm{i}} / \hat{\psi}_{\mathrm{R}}^2 \qquad k_{\mathrm{p}} = k_{\mathrm{i}} L_\sigma / r \tag{12}$$

where $k'_{\mathrm{i}} = 0.5$ p.u. is used in the following. The eigenvalues of the closed-loop system with the proposed gain design are shown in Fig. 12(b). A completely stable, well-damped, and comparatively robust system is achieved.

C. Stator-Resistance Adaptation

The speed adaptation law (5) drives the current estimation error $\tilde{i}_{\mathrm{q}}$ to zero in the steady state. The remaining nonzero component $\tilde{i}_{\mathrm{d}}$ in the direction of the flux estimate can be used for estimating one model parameter. For improved low-speed operation, the observer can be augmented with the stator-resistance adaptation law [3]

$$\hat{R}_{\mathrm{s}} = \int k_{\mathrm{R}} \hat{\boldsymbol{\psi}}_{\mathrm{R}}^{\mathrm{T}} \tilde{\boldsymbol{i}}_{\mathrm{s}} \mathrm{d}t \tag{13}$$

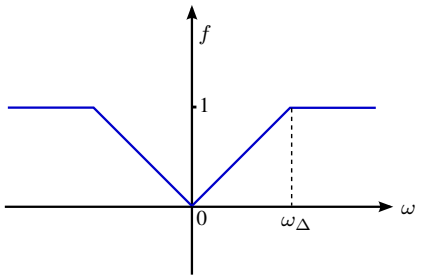

Fig. 4. Function f, which is used in (9) and (11).

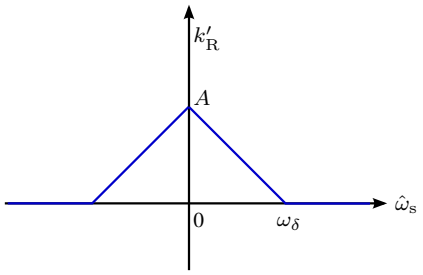

Fig. 5. Parameter k'_{R} as function of $\hat{\omega}_{\mathrm{s}}$.

which in estimated flux coordinates reduces to

$$\hat{R}_{\mathrm{s}} = \int k_{\mathrm{R}} \hat{\psi}_{\mathrm{R}} \tilde{i}_{\mathrm{d}} \mathrm{d}t \tag{14}$$

Unfortunately, the closed-loop dynamics of the augmented observer become very complex. Hence, instead of trying to derive exact analytical stability conditions, the stability analysis and the adaptation gain design is carried out using numerical methods in the following.

Furthermore, an approximate analytical stability condition based on the principle of the time-scale separation [5] is derived in Appendix C. In the approximation, the observer dynamics and the speed-adaptation loop are assumed to be much faster than the dynamics of the resistance-adaptation loop. Therefore, the observer can be assumed to be in quasi-steady state as seen from the slower resistance-adaptation loop. This approximation leads to the first-order closed-loop system

$$\frac{\mathrm{d}\hat{R}_{\mathrm{s}}}{\mathrm{d}t} = \alpha_{\mathrm{R}} (R_{\mathrm{s}} - \hat{R}_{\mathrm{s}}) \tag{15}$$

where the analytical expression for the approximate bandwidth α_{R} of the resistance adaptation can be found in Appendix C. Naturally, the adaptation gain should be chosen so that α_{R} is nonnegative.

Based on the approximate bandwidth α_{R} and the results of extensive numerical eigenvalue analysis and computer simulations of the full system, the sign of the stator-resistance adaptation gain k_{R} should depend on the stator frequency (at most operating points). Due to errors in measurements and in other parameters, the stator resistance can be estimated only when the rotor speed is low and the load is high [7], [23]. The adaptation should be disabled in the vicinity of no-load operation and at higher stator frequencies due to poor signal-to-noise ratio. The resistance adaptation is disabled when $i_{\mathrm{sq}} < 0.1$ p.u. and the adaptation gain k_{R} is made proportional to

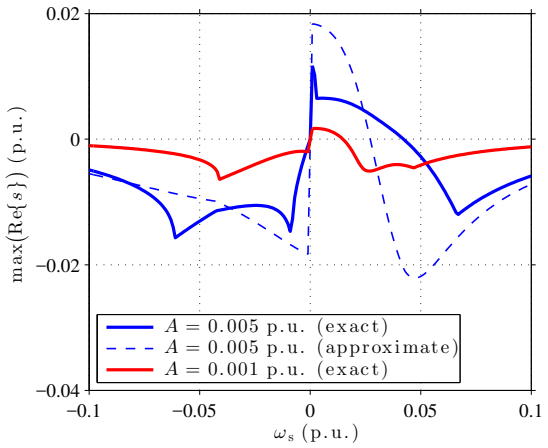

Fig. 6. Maximum real part of all eigenvalues of the closed-loop system matrix with the proposed gains and the stator-resistance adaptation. The numerically calculated eigenvalues are shown for $A = 0.005$ p.u. and for $A = 0.001$ p.u. Furthermore, the pole $s = -\alpha_\mathrm{R}$ corresponding to the approximate model is also shown for $A = 0.005$ p.u. The operating-point stator frequency is $\omega_{\mathrm{s}0} = -0.1 \ldots 0.1$ p.u. The rotor flux and the slip frequency are at their rated values. The stator-resistance adaptation causes an unstable region in the motoring mode in this operating point.

$|i_{\mathrm{sq}}|$. Furthermore, k_R is made to decrease linearly with the increasing stator frequency. The gain is realized as

$$k_\mathrm{R} = k'_\mathrm{R}(\hat{\omega}_\mathrm{s})\,\mathrm{sgn}(\hat{\omega}_\mathrm{s})|i_{\mathrm{sq}}| \tag{16}$$

where the function k'_R is shown in Fig. 5. The function can be expressed as

$$k'_\mathrm{R}(\hat{\omega}_\mathrm{s}) = \max\left\{A\left(1 - \frac{|\hat{\omega}_\mathrm{s}|}{\omega_\delta}\right), 0\right\} \tag{17}$$

where A and ω_δ are positive constants. In the following, $\omega_\delta = 0.25$ p.u. is selected.

The resistance adaptation causes an unstable region in the low-speed region, which is very difficult to avoid by means of gain scheduling. However, this unstable region can be made relatively narrow, if a low value for k'_R is used. As an example, the numerically calculated maximum real part of all eigenvalues at the rated flux and rated slip frequency are shown in Fig. 6 for $A = 0.005$ p.u. and $A = 0.001$ p.u. Furthermore, the pole $s = -\alpha_\mathrm{R}$ corresponding to the approximate model is also shown for $A = 0.005$ p.u. It can be seen that both the approximate model and the full linearized model predict an unstable region in the motoring mode, but there is clear discrepancy between these models. According to the approximate model, the size of the unstable region (i.e., zero crossings in the figure) does not depend on the magnitude of the resistance-adaptation gain, while the full linearized model shows dependency on the gain. In the following, $A = 0.005$ p.u. is selected, which corresponds to the unstable region of $0 \leq \omega_\mathrm{s} \leq 0.0422$ p.u. in the motoring mode according to Fig. 6. Since the rated slip frequency of the 2.2-kW IM is 0.0427 p.u., stable zero-speed operation under the rated load torque is theoretically possible, but this operating point is already very close to the unstable region.

It is worth mentioning that the unstable region in Fig. 6 could be avoided by choosing a smaller (or zero) $|k_\mathrm{R}|$ gain at the unstable operating points. However, since no exact analytical stability conditions exist, the stator-resistance adaptation gain should be iteratively tuned based on tedious numerical studies and trial-and-error tests. The load also affects the unstable operating region, which would further complicate the tuning procedure. Hence, the stator-resistance adaptation can be impractical or impossible to implement (especially in the case of general-purpose drives, where the motor is typically unknown) in the case of the speed-adaptive full-order observer.

IV. Benchmark Method: Reduced-Order Observer

The reduced-order flux observer proposed in [21] is used as a benchmark method in the experimental tests in Section VI. The observer structure in estimated rotor flux coordinates is

$$\frac{\mathrm{d}\hat{\boldsymbol{\psi}}_\mathrm{R}}{\mathrm{d}t} + \hat{\omega}_\mathrm{s}\boldsymbol{J}\hat{\boldsymbol{\psi}}_\mathrm{R} = \boldsymbol{e} + \boldsymbol{G}(\hat{\boldsymbol{e}} - \boldsymbol{e}) \tag{18}$$

where $\boldsymbol{G}$ is the observer gain matrix. The two expressions for back EMF induced by the rotor flux are

$$\boldsymbol{e} = \boldsymbol{u}_\mathrm{s} - \hat{R}_\mathrm{s}\boldsymbol{i}_\mathrm{s} - L_\sigma\frac{\mathrm{d}\boldsymbol{i}_\mathrm{s}}{\mathrm{d}t} - \hat{\omega}_\mathrm{s}L_\sigma\boldsymbol{J}\boldsymbol{i}_\mathrm{s} \tag{19a}$$

$$\hat{\boldsymbol{e}} = R_\mathrm{R}\boldsymbol{i}_\mathrm{s} - (\alpha\boldsymbol{I} - \hat{\omega}_\mathrm{m}\boldsymbol{J})\hat{\boldsymbol{\psi}}_\mathrm{R} \tag{19b}$$

An inherently sensorless observer is obtained by selecting the observer gain matrix $\boldsymbol{G}$ as

$$\boldsymbol{G} = \begin{bmatrix} g_1 & 0 \\ g_2 & 0 \end{bmatrix} \tag{20}$$

The general stabilizing gain corresponds to the gain components

$$g_1 = \frac{b\alpha - (c/\hat{\omega}_\mathrm{s} - \hat{\omega}_\mathrm{s})\hat{\omega}_\mathrm{m}}{\alpha^2 + \hat{\omega}_\mathrm{m}^2} \tag{21a}$$

$$g_2 = \frac{b\hat{\omega}_\mathrm{m} + (c/\hat{\omega}_\mathrm{s} - \hat{\omega}_\mathrm{s})\alpha}{\alpha^2 + \hat{\omega}_\mathrm{m}^2} \tag{21b}$$

which depend on the estimated speed. The observer is locally stable for all positive values of the design parameter b and c with accurate model parameters. The rotor speed is estimated using the slip relation.

The reduced-order observer is augmented with the stator-resistance adaptation as described in [21]. An advantage of the reduced-order observer (compared to the speed-adaptive full-order observer) is that the resistance adaptation can be more easily tuned based on the existing analytical stability conditions. The unstable regions appearing in the case of the full-order observer with resistance adaptation (illustrated in Fig. 6) are avoided.

V. Experimental Setup and Implementation

The proposed full-order observer gain design, the original gain design, and the benchmark method were compared by means of experiments. The 2.2-kW four-pole IM (cf. Section II) was used in the laboratory experiments. The IM was fed by a frequency converter controlled by a dSPACE DS1103 PPC/DSP board. A servo motor was used as a loading machine. The total moment of inertia of the experimental setup is 0.015 kgm^2. The speed was measured using an incremental encoder for monitoring purposes.

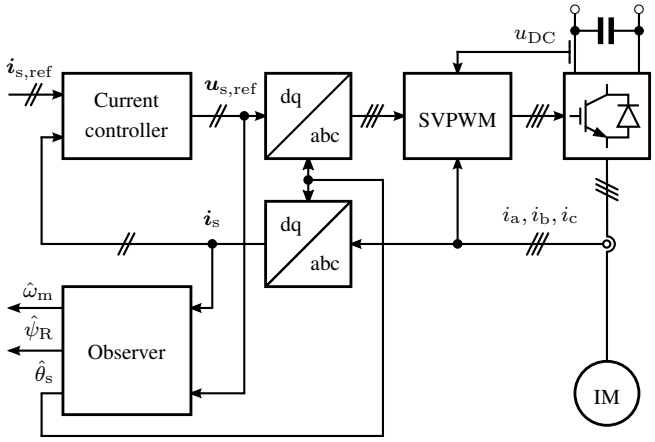

Fig. 7. Sensorless control system. The stator currents i_{a}, i_{b}, and i_{c} and the dc-link voltage u_{DC} are measured. The estimated flux angle is denoted by $\hat{\theta}_{\mathrm{s}}$. The components of the current reference $\boldsymbol{i}_{\mathrm{s,ref}}$ are used for controlling the flux and the torque. The control system also included the speed controller and flux-weakening controller (not shown).

A. Sensorless Control System

The speed-sensorless control algorithms were implemented in the dSPACE board. The block diagram of the sensorless control system is shown in Fig. 7. The block "Observer" represents either the speed-adaptive full-order observer or reduced-order observer. Both the observers are implemented in estimated rotor-flux coordinates. The space-vector pulse-width modulator (SVPWM) with compensation for inverter nonlinearities is used. The reference voltage $\boldsymbol{u}_{\mathrm{s,ref}}$ obtained from the current controller is fed to the flux observer. The speed controller and flux-weakening controller correspond to [24]. Furthermore, the magnetic saturation was modeled according to [24]. The sampling was synchronized to the SVPWM, and both the switching frequency and the sampling frequency were 5 kHz. For fair comparison, the other parts of the control algorithm (speed controller, current controller, SVPWM, magnetic-saturation model, etc.) and their tuning were kept the same for all the observers. The tuning of the reduced-order observer (in p.u. values since the motor is not the same) corresponds to that proposed in [21].

B. Compensation for Inverter Nonlinearities

The effect of inverter nonlinearities on the stator voltage is substantial at low speeds [17]. The most significant inverter nonlinearities, i.e., the dead-time effect and power device voltage drops, have to be compensated for [25]–[27]. Using phase a as an example, a compensated duty cycle for the pulsewidth modulator was evaluated as [21]

$$d_{\mathrm{a}} = d_{\mathrm{a,ref}} + \frac{2d_\delta}{\pi} \arctan\left(\frac{i_{\mathrm{a}}}{i_\delta}\right) \tag{22}$$

where $d_{\mathrm{a,ref}}$ is the ideal duty cycle obtained from the current controller and i_{a} is the phase current. The parameter $d_\delta = 0.011$ p.u. takes into account both the dead-time effect and the threshold voltage of the power devices, while the on-state slope resistance of the power devices is included in the stator-resistance estimate. The shape of the arctan function is determined by the parameter $i_\delta = 0.21$ p.u. The duty cycles of phases b and c were evaluated in a similar manner.

C. Digital Implementation of the Observer

At high speeds, the digital implementation of the observer has an important effect on the estimation accuracy and stability [22], [28], [29]. Good estimation accuracy at all stator frequencies can be achieved by implementing the observer in synchronous coordinates (where the quantities are dc in the steady state) in accordance with Fig. 7. If the observer were discretized using the forward Euler method, the discrete observer would become unstable at high speeds in any coordinate systems (however, the better the damping of the continuous-time design, the higher is the maximum stable operating frequency). Instead of the forward Euler method, the Tustin method could be used, but this method is computationally expensive. It is worth noticing that the observer system matrix $\hat{\boldsymbol{A}}$ is time varying: this matrix depends on $\hat{\omega}_{\mathrm{m}}$ and possibly also on non-constant parameter estimates.

Here, the semi-implicit (or symplectic) Euler method in synchronous coordinates is selected for both the observers [30], [31]. This method is even simpler to implement than the forward Euler method, but it preserves well the damping between the continuous-time and discrete-time domains.

VI. Experimental Results

A. Comparison With the Original Gains

Due to the voltage-model-like behavior at zero frequency, it was difficult to start the motor in the experiments from zero speed with the original gain selection. Hence, the motor was first started using the proposed gains and then switched to the original gains at nonzero frequency.

Fig. 8 shows the results of no-load speed reversals using the original and proposed gains. The speed reference was ramped from 0.06 p.u. to -0.06 p.u. and then reversed back to 0.06 p.u. within 3 s. The stator-resistance adaptation was disabled. It can be seen that the system with the original gains becomes unstable in the low-speed region. On the other hand, there are no problems when the proposed gains are used.

B. Comparison With the Reduced-Order Observer

1) Operation At Medium and Higher Speeds: Medium-speed operation is shown in Fig. 9. The speed reference was stepped to 0.5 p.u. at $t = 1$ s and stepped to zero at $t = 4$ s, and rated-load torque was applied at $t = 2$ s and removed at $t = 3$ s. Results did not show significant differences between the performance of the full-order and reduced-order observers at medium speeds (or even at low speeds, if the stator-resistance adaptation was disabled).

Fig. 10 shows the results of operation at higher speeds. The speed was stepped to 2 p.u. at $t = 0.5$ s and a 30% of the rated load was applied at $t = 1.5$ s. It can be seen that the reduced-order observer is more sensitive to noise (which originates particularly from the SVPWM operating at the border of the overmodulation region). It is worth noticing that the effect of the noise could be reduced by decreasing dynamic performance of the drive (i.e., by reducing the bandwidth of the speed controller).

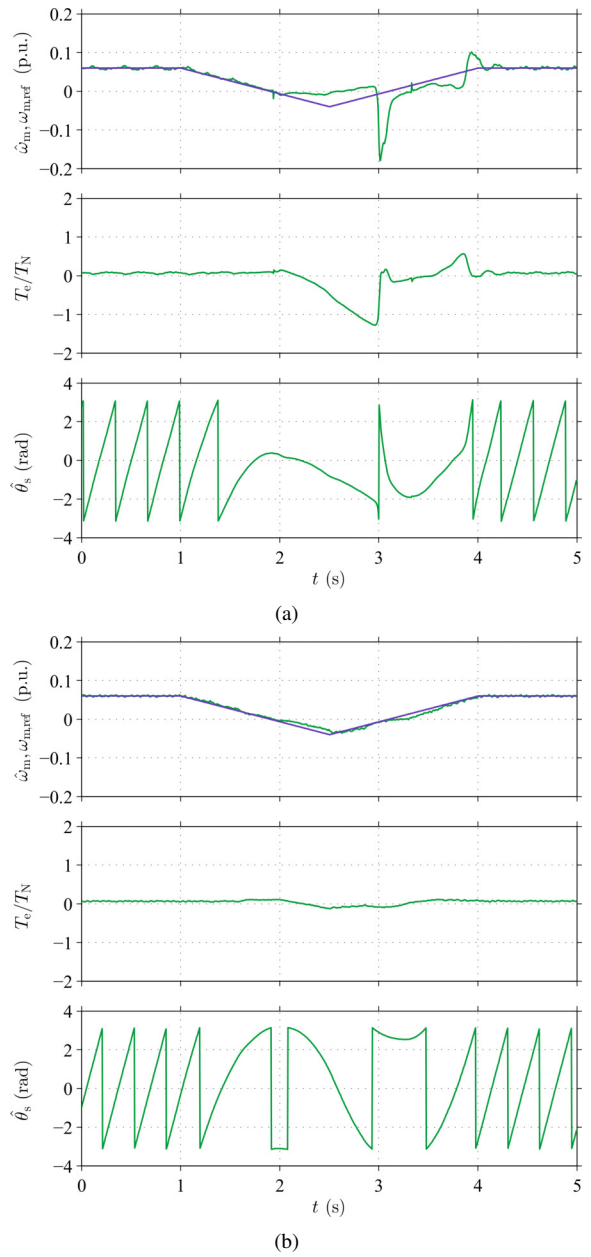

Fig. 8. Experimental results showing no-load speed reversals of the full-order observers: (a) original gains; (b) proposed gains. The first subplot shows the speed reference and the estimated speed, the second subplot shows the estimated torque, and the last subplot shows the estimated rotor-flux angle.

2) Stator-Resistance Adaptation at Lowest Speeds: Fig. 11 shows the experimental results of low-speed reversals. The rated load torque was stepwise applied at $t = 1$ s. The speed reference was slowly ramped from 0.06 p.u. to -0.06 p.u., and then back to 0.06 p.u. in 30 s. This test is very challenging, since motoring, plugging, and regenerating are gone through and the stator frequency is very low. Successful stator-resistance adaptation makes the system more robust against temperature changes, and it is possible to repeat the test without problems. It can be seen that the reduced-order observer augmented with the stator-resistance adaptation scheme works well.

When the augmented full-order observer is used, the system is stable, but there are visible oscillations in the stator resistance estimate $\hat{R}_\mathrm{s}$ after $t = 24$ s (as the drive enters the motoring mode), indicating a higher risk of instability. This agrees with the eigenvalue analysis shown in Fig. 6: the stator-resistance adaptation causes a narrow unstable region in the low-speed operation. Furthermore, when the parameter k'_R was increased, the oscillation in $\hat{R}_\mathrm{s}$ became worse.

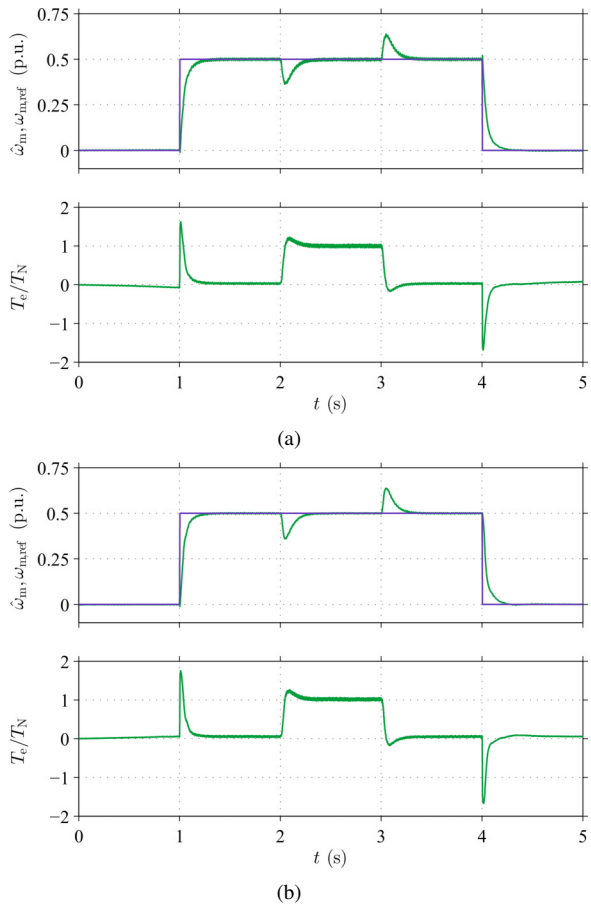

Fig. 9. Experimental results showing the medium-speed operation: (a) reduced-order observer; (b) full-order observer. The first subplot shows the speed reference and the estimated speed, the second subplot shows the estimated torque.

The persistent operation at zero stator frequency under load torque cannot be achieved; this is a fundamental limitation of sensorless IM drives [17]. Thus it is obvious that the speed reversals would become unstable if the speed ramps were made much slower (assuming that the maximum and minimum speeds remain the same). The maximum time that can be spent in the vicinity of zero stator frequency, without losing the stability of the drive, depends on the accuracy of the compensation for inverter nonlinearities and the accuracy of the parameter estimates (mainly on the accuracy of the inductance estimates if the stator-resistance adaptation is enabled in its stable region). However, a well-designed completely stable observer is a necessary precondition for stable operation.

Operation at zero speed under load condition is an easier test, since the stator frequency equals the nonzero slip frequency. In the case of the reduced-order observer with resistance adaptation, there are no theoretical limitations for

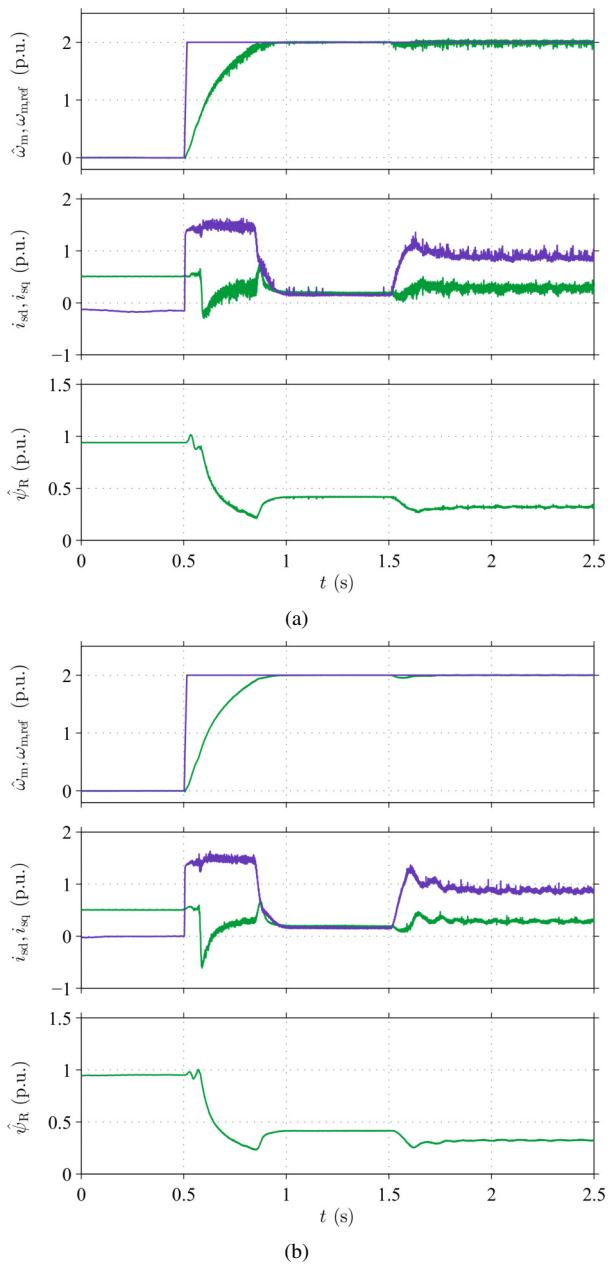

Fig. 10. Experimental results showing operation at higher speeds: (a) reduced-order observer; (b) full-order observer. The first subplot shows the speed reference and the estimated speed, the second subplot shows the current components in estimated rotor-flux coordinates, and the last subplot shows the estimated flux magnitude.

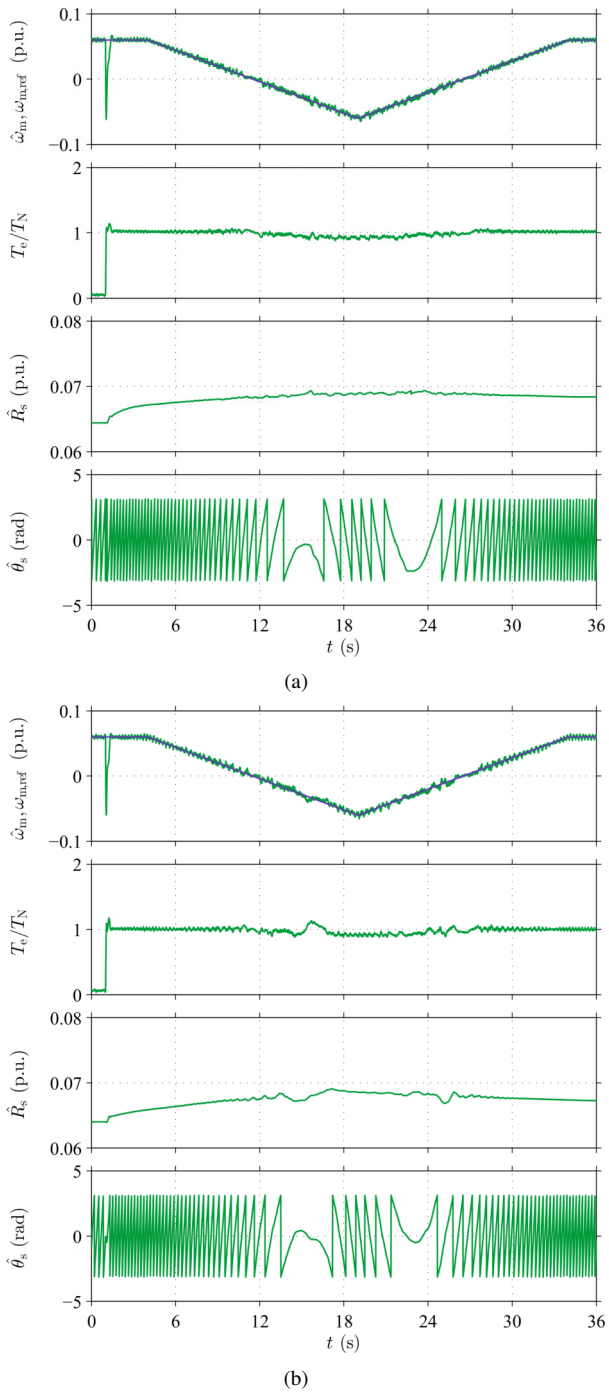

Fig. 11. Experimental results showing low-speed reversals with rated load torque: (a) reduced-order observer; (b) full-order observer. The first subplot shows the speed reference and the estimated speed, the second subplot shows the estimated torque, the third subplot shows the stator-resistance estimate, and the last subplot shows the estimated rotor flux angle.

this kind of operation, if ideal operating conditions are assumed [21]. The full-order observer with resistance adaptation, however, has an unstable region even in the case of ideal operating conditions, as discussed in Section III-C. Fig. 12 shows experimental results of zero-speed operation under the rated load torque for both the observer types. The load torque is stepped from zero to the rated torque at $t = 5$ s and stepped back to zero at $t = 55$ s. It can be seen that both the observers can be operated at zero speed under the rated load torque for a long time. However, as explained in Section III-C, the full-order observer operates very close to its unstable region in this operating point, which probably also increases the noise in the stator-resistance estimate. It can also be seen that the resistance estimates increase due to the rising temperature of the stator winding. Naturally, the inductance estimates and inverter nonlinearities play an important role also in this operating condition.

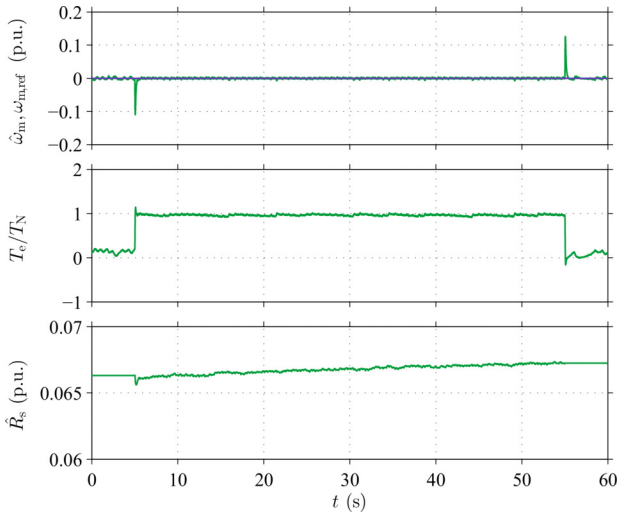

(a)

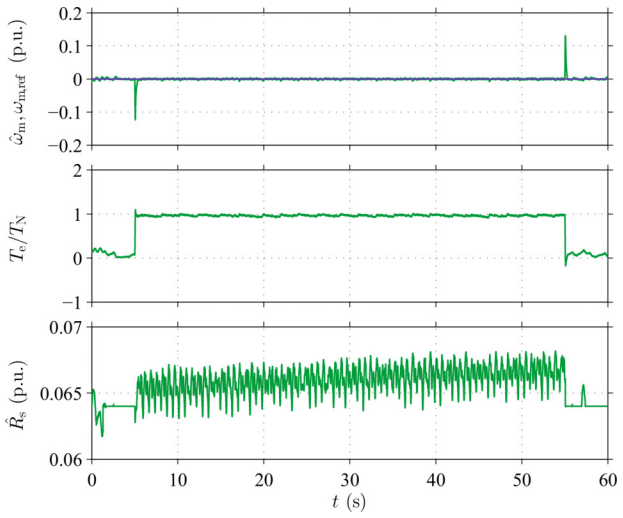

(b)

Fig. 12. Experimental results showing zero speed operation with rated load torque: (a) reduced-order observer; (b) full-order observer. The first subplot shows the speed reference and the estimated speed, the second subplot shows the estimated torque, the third subplot shows the stator-resistance estimate.

VII. Conclusions

The gain-scheduling design for the speed-adaptive full-order observer was proposed. In order to guarantee the complete stability with accurate model parameters, the gain design was based on the general stabilizing gain [9]. Compared to the original design in [9], the proposed gain design improves the robustness against model parameter errors at lowest speeds.

Furthermore, the full-order observer was augmented with the stator-resistance adaptation scheme. Based on extensive numerical eigenvalue analysis, the estimation-error dynamics of the augmented full-order observer are very difficult to completely stabilize (while the unstable region can be made very narrow by slowing down the dynamics of the resistance adaptation).

The full-order flux observer was compared with the reduced-order flux observer using experimental tests of a 2.2-kW IM drive. Experimental results indicate that the full-order flux observer has slightly better noise rejection at higher speeds. However, the reduced-order observer is more favorable at low speeds, since it can be augmented with the completely stable stator-resistance adaptation scheme.

Appendix A
Fluxes as State Variables

If the stator flux and the rotor flux are selected as state variables, the state-space representation becomes

$$\frac{\mathrm{d}}{\mathrm{d}t}\underbrace{\begin{bmatrix}\boldsymbol{\psi}_\mathrm{s}\\ \boldsymbol{\psi}_\mathrm{R}\end{bmatrix}}_{\boldsymbol{x}'} = \underbrace{\begin{bmatrix}-\frac{R_\mathrm{s}}{L_\sigma}\boldsymbol{I}-\hat{\omega}_\mathrm{s}\boldsymbol{J} & \frac{R_\mathrm{s}}{L_\sigma}\boldsymbol{I}\\ \frac{(1-\sigma)\alpha}{\sigma}\boldsymbol{I} & -\frac{\alpha}{\sigma}\boldsymbol{I}-(\hat{\omega}_\mathrm{s}-\omega_\mathrm{m})\boldsymbol{J}\end{bmatrix}}_{\boldsymbol{A}'}\begin{bmatrix}\boldsymbol{\psi}_\mathrm{s}\\ \boldsymbol{\psi}_\mathrm{R}\end{bmatrix} + \underbrace{\begin{bmatrix}\boldsymbol{I}\\ \boldsymbol{O}\end{bmatrix}}_{\boldsymbol{B}'}\boldsymbol{u}_\mathrm{s} \tag{23a}$$

$$\boldsymbol{i}_\mathrm{s} = \underbrace{\begin{bmatrix}\frac{1}{L_\sigma} & -\frac{1}{L_\sigma}\end{bmatrix}}_{\boldsymbol{C}'}\begin{bmatrix}\boldsymbol{\psi}_\mathrm{s}\\ \boldsymbol{\psi}_\mathrm{R}\end{bmatrix} \tag{23b}$$

where the total leakage factor is $\sigma = L_\sigma/(L_\mathrm{M}+L_\sigma)$. An observer

$$\frac{\mathrm{d}\hat{\boldsymbol{x}}'}{\mathrm{d}t} = \hat{\boldsymbol{A}}'\hat{\boldsymbol{x}}' + \boldsymbol{B}'\boldsymbol{u}_\mathrm{s} + \boldsymbol{K}'(\boldsymbol{i}_\mathrm{s}-\hat{\boldsymbol{i}}_\mathrm{s}) \tag{24a}$$

$$\hat{\boldsymbol{i}}_\mathrm{s} = \boldsymbol{C}'\hat{\boldsymbol{x}}' \tag{24b}$$

is equivalent to the observer in (2) if

$$\boldsymbol{K}' = \begin{bmatrix}L_\sigma\boldsymbol{I} & \boldsymbol{I}\\ \boldsymbol{O} & \boldsymbol{I}\end{bmatrix}\boldsymbol{K} \tag{25}$$

holds for the observer gain matrices [2]. Hence, the stabilizing observer gains in (6) are transformed to

$$\boldsymbol{K}'_\mathrm{s} = (\alpha l-\hat{R}_\mathrm{s})\boldsymbol{I} + \hat{\omega}_\mathrm{m} l\boldsymbol{J} \tag{26a}$$

$$\boldsymbol{K}'_\mathrm{r} = (R_\mathrm{R}-r+\alpha l)\boldsymbol{I} + (\hat{\omega}_\mathrm{m} l - x)\boldsymbol{J} \tag{26b}$$

It can be seen that choosing $l=0$ leads to $\boldsymbol{K}'_\mathrm{s} = -\hat{R}_\mathrm{s}\boldsymbol{I}$ (for any r and x), i.e., the dynamics of $\hat{\boldsymbol{\psi}}_\mathrm{s}$ become equal to those of the pure voltage model [2]. Hence, selecting $l=0$ should be avoided.

Appendix B
Linearized Model

Accurate parameter estimates (except $\hat{R}_\mathrm{s}$) are assumed. Using (1) and (2), the linearized dynamics from the inputs $\tilde{\omega}_\mathrm{m}$ and $\tilde{R}_\mathrm{s}$ to the output $\tilde{\boldsymbol{i}}_\mathrm{s}$ become

$$\frac{\mathrm{d}\tilde{\boldsymbol{x}}}{\mathrm{d}t} = \underbrace{\begin{bmatrix}-\frac{R_\sigma}{L_\sigma}\boldsymbol{I}-\omega_\mathrm{s0}\boldsymbol{J}-\boldsymbol{K}_\mathrm{s0} & \frac{1}{L_\sigma}(\alpha\boldsymbol{I}-\omega_\mathrm{m0}\boldsymbol{J})\\ R_\mathrm{R}\boldsymbol{I}-\boldsymbol{K}_\mathrm{r0} & -\alpha\boldsymbol{I}-\omega_\mathrm{r0}\boldsymbol{J}\end{bmatrix}}_{\boldsymbol{A}_\mathrm{e}}\tilde{\boldsymbol{x}} + \underbrace{\begin{bmatrix}-\frac{1}{L_\sigma}\boldsymbol{J}\boldsymbol{\psi}_\mathrm{R0} & -\frac{1}{L_\sigma}\boldsymbol{i}_\mathrm{s0}\\ \boldsymbol{J}\boldsymbol{\psi}_\mathrm{R0} & 0\end{bmatrix}}_{\boldsymbol{B}_\mathrm{e}}\begin{bmatrix}\tilde{\omega}_\mathrm{m}\\ \tilde{R}_\mathrm{s}\end{bmatrix} \tag{27a}$$

$$\tilde{\boldsymbol{i}}_\mathrm{s} = \boldsymbol{C}\tilde{\boldsymbol{x}} \tag{27b}$$

where $\tilde{\boldsymbol{x}} = \boldsymbol{x}-\hat{\boldsymbol{x}}$ is the estimation error of the state vector and other estimation errors are defined similarly. Operating

point quantities are marked with the subscript 0 and $\omega_{\mathrm{r}0} = \omega_{\mathrm{s}0} - \omega_{\mathrm{m}0}$ is the angular slip frequency. The linearized speed and resistance adaptation laws are

$$\frac{\mathrm{d}\tilde{\omega}_{\mathrm{m}}}{\mathrm{d}t} = \boldsymbol{\psi}_{\mathrm{R}0}\boldsymbol{J}\left(k_{\mathrm{p}0}\frac{\mathrm{d}\tilde{\boldsymbol{i}}_{\mathrm{s}}}{\mathrm{d}t} + k_{\mathrm{i}0}\tilde{\boldsymbol{i}}_{\mathrm{s}}\right) \tag{28a}$$

$$\frac{\mathrm{d}\tilde{R}_{\mathrm{s}}}{\mathrm{d}t} = k_{\mathrm{R}0}\boldsymbol{\psi}_{\mathrm{R}0}^{\mathrm{T}}\tilde{\boldsymbol{i}}_{\mathrm{s}} \tag{28b}$$

Substituting

$$\frac{\mathrm{d}\tilde{\boldsymbol{i}}_{\mathrm{s}}}{\mathrm{d}t} = \boldsymbol{A}_{\mathrm{e}11}\tilde{\boldsymbol{i}}_{\mathrm{s}} + \boldsymbol{A}_{\mathrm{e}12}\tilde{\boldsymbol{\psi}}_{\mathrm{R}} + \boldsymbol{B}_{\mathrm{e}11}\tilde{\omega}_{\mathrm{m}} + \boldsymbol{B}_{\mathrm{e}12}\tilde{R}_{\mathrm{s}} \tag{29}$$

into (28a) yields

$$\begin{aligned}\frac{\mathrm{d}}{\mathrm{d}t}\begin{bmatrix}\tilde{\omega}_{\mathrm{m}}\\ \tilde{R}_{\mathrm{s}}\end{bmatrix} &= \begin{bmatrix}k_{\mathrm{p}0}\boldsymbol{\psi}_{\mathrm{R}0}^{\mathrm{T}}\boldsymbol{J}\boldsymbol{B}_{\mathrm{e}11} & k_{\mathrm{p}0}\boldsymbol{\psi}_{\mathrm{R}0}^{\mathrm{T}}\boldsymbol{J}\boldsymbol{B}_{\mathrm{e}12}\\ 0 & 0\end{bmatrix}\begin{bmatrix}\tilde{\omega}_{\mathrm{m}}\\ \tilde{R}_{\mathrm{s}}\end{bmatrix}\\ &\quad + \begin{bmatrix}k_{\mathrm{p}0}\boldsymbol{\psi}_{\mathrm{R}0}^{\mathrm{T}}\boldsymbol{J}\boldsymbol{A}_{\mathrm{e}11} + k_{\mathrm{i}0}\boldsymbol{\psi}_{\mathrm{R}0}^{\mathrm{T}}\boldsymbol{J} & k_{\mathrm{p}0}\boldsymbol{\psi}_{\mathrm{R}0}^{\mathrm{T}}\boldsymbol{J}\boldsymbol{A}_{\mathrm{e}12}\\ k_{\mathrm{R}0}\boldsymbol{\psi}_{\mathrm{R}0}^{\mathrm{T}} & 0\end{bmatrix}\tilde{\boldsymbol{x}}\end{aligned} \tag{30}$$

where $\boldsymbol{A}_{\mathrm{e}11}$, $\boldsymbol{A}_{\mathrm{e}12}$, $\boldsymbol{B}_{\mathrm{e}11}$, and $\boldsymbol{B}_{\mathrm{e}12}$ are the corresponding submatrices of $\boldsymbol{A}_{\mathrm{e}}$ and $\boldsymbol{B}_{\mathrm{e}}$. Using (27) and (30), the eigenvalues of the closed-loop estimation error dynamics can be evaluated. If the stator-resistance adaptation is disabled, its effect can be easily dropped out from the above equations.

As described in Sections III-B and III-C, the gains $\boldsymbol{K}$, k_{p}, k_{i}, and k_{R} are functions of the operating point. If accurate parameter estimates are assumed, $\tilde{\boldsymbol{x}}_0 = 0$ and $\hat{\omega}_{\mathrm{m}0} = \omega_{\mathrm{m}0}$ hold at the operating point. Therefore, the linearized model is valid, even if the gains are functions of the operating point. Furthermore, the general stabilizing gain (6) guarantees the complete stability (if the stator-resistance adaptation is disabled).

As far as accurate parameter estimates are assumed, the linearized estimation-error dynamics of the speed-adaptive full-order observer (or the reduced-order observer [21]) do not couple with the linearized control-error dynamics. Hence, only the estimation-error dynamics are considered here. The stability of the linearized estimation-error dynamics is a necessary (but not sufficient) condition for the local stability of the whole drive system. It is worth noticing that this separation does not hold for all estimators (e.g., for a statically-compensated voltage model [18]) or it does not hold if parameter errors are considered [1].

Appendix C
Approximate Resistance-Adaptation Dynamics

Based on (27), the transfer function from the stator-resistance estimation error $\tilde{R}_{\mathrm{s}}(s)$ to the estimation error $\tilde{i}_{\mathrm{d}}(s)$ of the d-axis current becomes

$$G_{\mathrm{d}}(s) = -\frac{1}{L_\sigma}\frac{A_1(s)B_1(s) + A_2(s)B_2(s)}{A_1^2(s) + A_2^2(s)} \tag{31}$$

where

$$B_1(s) = si_{\mathrm{sd}0} + i_{\mathrm{sd}0}\alpha - i_{\mathrm{sq}0}\omega_{\mathrm{r}0} \tag{32a}$$

$$B_2(s) = si_{\mathrm{sq}0} + i_{\mathrm{sq}0}\alpha + i_{\mathrm{sd}0}\omega_{\mathrm{r}0} \tag{32b}$$

$$\begin{aligned}A_1(s) &= s^2 + s\left(\frac{R_\sigma}{L_\sigma} + \alpha + k_{\mathrm{sd}0}\right) - \omega_{\mathrm{r}0}(\omega_{\mathrm{s}0} + k_{\mathrm{sq}0})\\ &\quad + \alpha k_{\mathrm{sd}0} + \frac{\alpha(R_{\mathrm{s}} + k_{\mathrm{rd}0}) + k_{\mathrm{rq}0}\omega_{\mathrm{m}0}}{L_\sigma}\end{aligned} \tag{32c}$$

$$\begin{aligned}A_2(s) &= s(\omega_{\mathrm{r}0} + \omega_{\mathrm{s}0} + k_{\mathrm{sq}0}) + \alpha(\omega_{\mathrm{s}0} + k_{\mathrm{sq}0}) + \omega_{\mathrm{r}0}k_{\mathrm{sd}0}\\ &\quad + \frac{\omega_{\mathrm{s}0}R_\sigma + \alpha k_{\mathrm{rq}0} - \omega_{\mathrm{m}0}(R_{\mathrm{s}} + k_{\mathrm{rd}0})}{L_\sigma}\end{aligned} \tag{32d}$$

The effect of the speed-adaptation loop will be omitted in the following. The resulting closed-loop resistance-adaptation dynamics are still complex,

$$\frac{\hat{R}_{\mathrm{s}}(s)}{R_{\mathrm{s}}(s)} = \frac{K(s)G_{\mathrm{d}}(s)}{1 + K(s)G_{\mathrm{d}}(s)} \tag{33}$$

where $K(s) = k_{\mathrm{R}0}\psi_{\mathrm{R}0}/s$ is the transfer function corresponding to the adaptation law (14). Hence, general analytical stability conditions for the speed-adaptive full-order observer augmented with the stator-resistance adaptation are difficult to derive. If the observer dynamics are assumed to be in quasi-steady state, the resistance-estimation dynamics reduce to

$$\frac{\hat{R}_{\mathrm{s}}(s)}{R_{\mathrm{s}}(s)} = \frac{\alpha_{\mathrm{R}}}{s + \alpha_{\mathrm{R}}} \tag{34}$$

where the approximate bandwidth is

$$\alpha_{\mathrm{R}} = k_{\mathrm{R}0}\psi_{\mathrm{R}0}G_{\mathrm{d}}(0) \tag{35}$$

The stability condition based on this approximation is $k_{\mathrm{R}0}[A_1(0)B_1(0) + A_2(0)B_2(0)] < 0$.

References

[1] L. Harnefors and M. Hinkkanen, "Stabilization methods for sensorless induction motor drives—a survey," *IEEE J. Emerg. Sel. Topics Power Electron.*, 2013, early access.

[2] M. Hinkkanen, "Analysis and design of full-order flux observers for sensorless induction motors," *IEEE Trans. Ind. Electron.*, vol. 51, no. 5, pp. 1033–1040, Oct. 2004.

[3] H. Kubota, K. Matsuse, and T. Nakano, "DSP-based speed adaptive flux observer of induction motor," *IEEE Trans. Ind. Appl.*, vol. 29, no. 2, pp. 344–348, Mar./Apr. 1993.

[4] L. Harnefors and H.-P. Nee, "Full-order observers for flux and parameter estimation of induction motors," in *Proc. EPE'97*, vol. 3, Trondheim, Norway, Sept. 1997, pp. 375–381.

[5] H. Hofmann and S. R. Sanders, "Speed-sensorless vector torque control of induction machines using a two-time-scale approach," *IEEE Trans. Ind. Appl.*, vol. 34, no. 1, pp. 169–177, Jan./Feb. 1998.

[6] G. Guidi and H. Umida, "A novel stator resistance estimation method for speed-sensorless induction motor drives," *IEEE Trans. Ind. Appl.*, vol. 36, no. 6, pp. 1619–1627, Nov./Dec. 2000.

[7] H. Tajima, G. Guidi, and H. Umida, "Consideration about problems and solutions of speed estimation method and parameter tuning for speed-sensorless vector control of induction motor drives," *IEEE Trans. Ind. Appl.*, vol. 38, no. 5, pp. 1282–1289, Sept./Oct. 2002.

[8] M. Saejia and S. Sangwongwanich, "Averaging analysis approach for stability analysis of speed-sensorless induction motor drives with stator resistance estimation," *IEEE Trans. Ind. Electron.*, vol. 53, no. 1, pp. 162–177, Feb. 2006.

[9] S. Sangwongwanich, S. Suwankawin, S. Po-ngam, and S. Koonlaboon, "A unified speed estimation design framework for sensorless ac motor drives based on positive-real property," in *Proc. PCC-Nagoya'07*, Nagoya, Japan, Apr. 2007, pp. 1111–1118.

[10] I. Vicente, A. Endemaño, X. Garin, and M. Brown, "Comparative study of stabilising methods for adaptive speed sensorless full-order observers with stator resistance estimation," *IET Control Theory & Appl.*, vol. 4, no. 6, pp. 993–1004, 2010.

[11] M. S. Zaky, "Stability analysis of speed and stator resistance estimators for sensorless induction motor drives," *IEEE Trans. Ind. Electron.*, vol. 59, no. 2, pp. 858–870, Feb. 2012.

[12] S. Maiti, V. Verma, C. Chakraborty, and Y. Hori, "An adaptive speed sensorless induction motor drive with artificial neural network for stability enhancement," *IEEE Trans. Ind. Informat.*, vol. 8, no. 4, pp. 757–766, Nov. 2012.

[13] S. A. Davari, D. A. Khaburi, F. Wang, and R. M. Kennel, "Using full order and reduced order observers for robust sensorless predictive torque control of induction motors," *IEEE Trans. Power Electron.*, vol. 27, no. 7, pp. 3424–3433, July 2012.

[14] B. Chen, W. Yao, K. Wang, K. Lee, and Z. Lu, "Comparative analysis of feedback gains for adaptive full-order observers in sensorless induction motor drives," in *Proc. IEEE ECCE 2013*, Denver, CO, Sept. 2013, pp. 3481–3487.

[15] S. Jafarzadeh, C. Lascu, and M. S. Fadali, "Square root unscented Kalman filters for state estimation of induction motor drives," *IEEE Trans. Ind. Appl.*, vol. 49, no. 1, pp. 92–99, Jan./Feb. 2013.

[16] F. Alonge, F. D'Ippolito, and A. Sferlazza, "Sensorless control of induction-motor drive based on robust Kalman filter and adaptive speed estimation," *IEEE Trans. Ind. Electron.*, vol. 61, no. 3, pp. 1444–1453, Mar. 2014.

[17] J. Holtz and J. Quan, "Sensorless vector control of induction motors at very low speed using a nonlinear inverter model and parameter identification," *IEEE Trans. Ind. Appl.*, vol. 38, no. 4, pp. 1087–1095, July/Aug. 2002.

[18] L. Harnefors and R. Ottersten, "Regeneration-mode stabilization of the 'statically compensated voltage model'," *IEEE Trans. Ind. Electron.*, vol. 54, no. 2, pp. 818–824, Apr. 2007.

[19] C. Lascu, I. Boldea, and F. Blaabjerg, "Very-low-speed variable-structure control of sensorless induction machine drives without signal injection," *IEEE Trans. Ind. Appl.*, vol. 41, no. 2, pp. 591–598, Mar./Apr. 2005.

[20] L. Harnefors and M. Hinkkanen, "Complete stability of reduced-order and full-order observers for sensorless IM drives," *IEEE Trans. Ind. Electron.*, vol. 55, no. 3, pp. 1319–1329, Mar. 2008.

[21] M. Hinkkanen, L. Harnefors, and J. Luomi, "Reduced-order flux observers with stator-resistance adaptation for speed-sensorless induction motor drives," *IEEE Trans. Ind. Electron.*, vol. 25, no. 5, pp. 1173–1183, May 2010.

[22] G. C. Verghese and S. R. Sanders, "Observers for flux estimation in induction machines," *IEEE Trans. Ind. Electron.*, vol. 35, no. 1, pp. 85–94, Feb. 1988.

[23] J. L. Zamora and A. García-Cerrada, "Online estimation of the stator parameters in an induction motor using only voltage and current measurements," *IEEE Trans. Ind. Appl.*, vol. 36, no. 3, pp. 805–816, May/June 2000.

[24] Z. Qu, M. Ranta, M. Hinkkanen, and J. Luomi, "Loss-minimizing flux level control of induction motor drives," *IEEE Trans. Ind. Appl.*, vol. 48, no. 3, pp. 952–961, May/June 2012.

[25] J. K. Pedersen, F. Blaabjerg, J. W. Jensen, and P. Thogersen, "An ideal PWM-VSI inverter with feedforward and feedback compensation," in *Proc. EPE'93*, vol. 4, Brighton, U.K., Sep. 1993, pp. 312–318.

[26] J.-W. Choi and S.-K. Sul, "Inverter output voltage synthesis using novel dead time compensation," *IEEE Trans. Power Electron.*, vol. 11, no. 2, pp. 221–227, Mar. 1996.

[27] G. Pellegrino, R. I. Bojoi, P. Guglielmi, and F. Cupertino, "Accurate inverter error compensation and related self-commissioning scheme in sensorless induction motor drives," *IEEE Trans. Ind. Appl.*, vol. 46, no. 5, pp. 1970–1978, Sep./Oct. 2010.

[28] C. P. Bottura, J. L. Silvino, and P. de Resende, "A flux observer for induction machines based on a time-variant discrete model," *IEEE Trans. Ind. Appl.*, vol. 29, no. 2, pp. 349–354, Mar./Apr. 1993.

[29] M. Hinkkanen and J. Luomi, "Digital implementation of full-order flux observers for induction motors," in *Proc. EPE-PEMC'02*, Cavtat and Dubrovnik, Croatia, Sept. 2002, CD-ROM.

[30] J. Niiranen, "Fast and accurate symmetric Euler algorithm for electromechanical simulations," in *Proc. Elecrimacs'99*, vol. 1, Lisboa, Portugal, Sept. 1999, pp. 71–78.

[31] M. Hinkkanen and J. Luomi, "Parameter sensitivity of full-order flux observers for induction motors," *IEEE Trans. Ind. Appl.*, vol. 39, no. 4, pp. 1127–1135, July/Aug. 2003.

Zengcai Qu received the B.Sc. in electrical engineering and automation in Shanghai Jiao Tong University, Shanghai, China in 2007, and M.Sc. degree in Space Science and Technology from Lulea University of Technology, Kiruna, Sweden and Helsinki University of Technology, Espoo, Finland in 2009.

Since 2009, he is currently working towards the Ph.D. degree in Aalto University, Espoo, Finland. His research interest is efficiency control and sensorless control of electric drives.

Marko Hinkkanen (M'06-SM'13) received the M.Sc.(Eng.) and D.Sc.(Tech.) degrees from Helsinki University of Technology, Espoo, Finland, in 2000 and 2004, respectively.

Since 2000, he has been with Helsinki University of Technology (part of Aalto University, Espoo, since 2010). He is currently an Assistant Professor (in tenure track) with the Aalto University School of Electrical Engineering. His research interests include power-electronic converters, electric machines, and electric drives.

Lennart Harnefors (S'93–M'97–SM'07) was born in 1968 in Eskilstuna, Sweden. He received the M.Sc., Licentiate, and Ph.D. degrees in electrical engineering from the Royal Institute of Technology (KTH), Stockholm, Sweden, and the Docent (D.Sc.) degree in industrial automation from Lund University, Lund, Sweden, in 1993, 1995, 1997, and 2000, respectively. From 1994 to 2005, he was with Mälardalen University, Västerås, Sweden, where he, in 2001, was appointed Professor of electrical engineering. From 2001 to 2005, he was, in addition, a part-time Visiting Professor of electrical drives with Chalmers University of Technology, Göteborg, Sweden. Since 2005, he has been with ABB, currently as a Senior Principal Scientist at Corporate Research, Västerås, Sweden. He is also part-time with KTH as an Adjunct Professor of power electronics. His research interests include analysis and control of power electronic systems, particularly grid-connected converters and ac drives.

Prof. Harnefors was the recipient of the 2000 ABB Gunnar Engström Energy Award and the 2002 IEEE TRANSACTIONS ON INDUSTRIAL ELECTRONICS Best Paper Award. He is an Associate Editor of the IEEE TRANSACTIONS ON INDUSTRIAL ELECTRONICS, a member of the Editorial Board of *IET Electric Power Applications*, and a member of the Executive Council and the International Scientific Committee of the European Power Electronics and Drives Association (EPE).